nature communications

Article

https://doi.org/10.1038/s41467-024-54372-1

Evolutionary changes leading to efficient glymphatic circulation in the mammalian brain

Received: 9 December 2023

Accepted: 5 November 2024

Narufumi Kameya[1,5], Itsuki Sakai[2,5], Kengo Saito[1], Toshihide Hamabe-Horiike[1], Yohei Shinmyo[1], Mitsutoshi Nakada[3,4], Satoru Okuda[2,3] & Hiroshi Kawasaki[1,3]

The functional significance of the morphological and genetic changes that occurred in the brain during evolution is not fully understood. Here we show the relationships between evolutionary changes of the brain and glymphatic circulation. We establish a mathematical model to simulate glymphatic circulation in the cerebral hemispheres, and our results show that cortical neurons accumulate in areas of the cerebral hemispheres where glymphatic circulation is highly efficient. We also find that cortical folds markedly enhance the efficiency of glymphatic circulation in the cerebral hemispheres. Furthermore, our in vivo study using ferrets reveals sulcus-dominant cerebrospinal fluid (CSF) influx, which enhances the efficiency of glymphatic circulation in the enlarged cerebral hemispheres of gyrencephalic brains. Sulcus-dominant CSF influx is mediated by preferential expression of aquaporin-4 in sulcal regions, and similar expression patterns of aquaporin-4 are also found in human cerebral hemispheres. These results indicate that evolutionary changes in the cerebral hemispheres are related to improved efficiency of glymphatic circulation. It seems plausible that the efficiency of glymphatic circulation is an important factor determining the evolutionary trajectory of the cerebral hemispheres.

The brain has changed drastically during evolution[1–7]. Neurons and glial cells in the cerebral hemispheres have increased in number, and as a result, the cerebral hemispheres have markedly expanded[8,9]. Neurons have accumulated close to the surface of the cerebral hemispheres, forming gray matter (i.e., the cerebral cortex), and white matter consisting of axons and myelin occupies the region under gray matter[10]. Furthermore, folds called gyri and sulci have appeared on the surface of the mammalian cerebral hemispheres[4,5]. It is believed that these evolutionary changes in the cerebral hemispheres are crucial for acquiring higher brain functions[2,6,7,11]. Indeed, abnormalities of the cerebral cortex and cortical folding are associated with severe brain dysfunction in human patients[12–16]. Recent studies have uncovered the molecular mechanisms regulating the formation of the cerebral cortex and cortical folding, and the biological roles of these evolutionary changes are an important area for future investigation[17–20].

The glymphatic system is a recently identified circulation system for cerebrospinal fluid (CSF)[21,22]. The CSF in the subarachnoid space flows into the parenchyma of the brain through the perivascular space[22]. The perivascular space is covered with astrocytic endfeet, and aquaporin-4 (AQP4) expressed on astrocytic endfeet mediates CSF

---

[1]Department of Medical Neuroscience, Graduate School of Medical Sciences, Kanazawa University, Ishikawa, Japan. [2]Nano Life Science Institute, Kanazawa University, Ishikawa, Japan. [3]Sapiens Life Sciences, Evolution and Medicine Research Center, Kanazawa University, Ishikawa, Japan. [4]Department of Neurosurgery, Graduate School of Medical Sciences, Kanazawa University, Ishikawa, Japan. [5]These authors contributed equally: Narufumi Kameya, Itsuki Sakai. e-mail: satokuda@staff.kanazawa-u.ac.jp; kawasaki@med.kanazawa-u.ac.jp

influx into the parenchyma[23,24]. The CSF mixes with the interstitial fluid in the parenchyma, and the mixture leaves through the venous perivascular space, facilitating the clearance of waste in the parenchyma[21]. It has been proposed that the impairment of the glymphatic system is involved in the pathogenesis of various diseases such as Alzheimer's disease, traumatic injury, and brain stroke[25–30]. Although these studies have highlighted the biological importance of the glymphatic system, the changes in the glymphatic system that have occurred during evolution are largely unknown because most studies have been carried out using mice[21,22].

The cerebral hemispheres have markedly expanded during evolution, and along with this expansion, it seemed possible that CSF influx from the brain surface could have become inefficient in deep regions of the enlarged cerebral hemispheres. Alternatively, enlarged cerebral hemispheres may have some additional features that enhance glymphatic circulation. Therefore, to examine glymphatic circulation in the enlarged cerebral hemispheres of gyrencephalic brains, here we mathematically investigated glymphatic circulation in the cerebral hemispheres of mice, monkeys, and humans. Our results showed that glymphatic circulation is highly efficient in the area corresponding to gray matter in the cerebral hemispheres. We also found that glymphatic circulation was more efficient in cerebral hemispheres with cortical folds than in those without cortical folds. Furthermore, to investigate glymphatic circulation in vivo, we injected a CSF tracer into the subarachnoid space of the ferret brain, which has relatively large cerebral hemispheres with cortical folds. We found that CSF influx was more prominent at sulci than at gyri in ferret cerebral hemispheres. This sulcus-dominant CSF influx was not observed in mouse cerebral hemispheres. Importantly, we obtained results which suggest that human cerebral hemispheres also have sulcus-dominant CSF influx. Our findings may indicate that evolutionary changes in the cerebral hemispheres have proceeded in a way that facilitated efficient glymphatic circulation.

Results

Mathematical modeling of glymphatic circulation in the mouse cerebral hemispheres

To quantitatively examine the efficiency of CSF influx into the cerebral hemispheres, we injected FITC-labeled 3 kDa dextran, a CSF tracer, into the cisterna magna of adult mice. The mouse brains were dissected 2 h later (Fig. 1a), and coronal sections were prepared (Fig. 1b). Consistent with previous studies[22,24], tracer signals were observed close to the brain surface (Fig. 1b), suggesting that CSF flows into the parenchyma from the brain surface.

We measured the intensities of tracer signals in coronal sections. We then made a mathematical model assuming that CSF follows the diffusion equation within the brain parenchyma (Supplementary Fig. 1, small white arrows) and that glymphatic circulation in the cerebral hemispheres is under a steady state (See Supplementary Method for details). We next fitted the model (Supplementary Fig. 1) to the measured tracer signal values and obtained the D/A value with a minimum mean square error of signal intensities (hereafter referred to as $(D/A)^*$) (Fig. 1c, arrow). Here, D is the diffusion coefficient of the diffusion equation, and A is the emission coefficient of CSF efflux. Using $(D/A)^*$, we simulated the spatial patterns of CSF solute concentrations in the mouse brain (see Supplementary Method for details), and we found

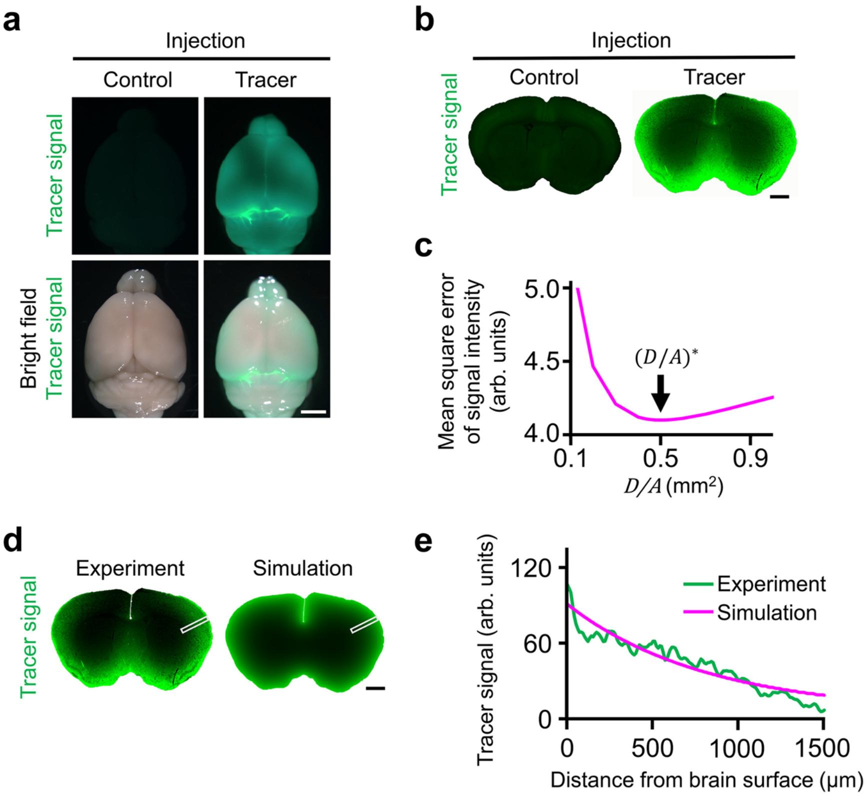

Fig. 1 | Mathematical modeling of glymphatic circulation in mouse cerebral hemispheres. a Mouse brain injected with or without a CSF tracer. Dorsal views are shown. **b** Coronal sections of the mouse brains injected with or without a CSF tracer. **c** The relationship between D/A and mean square errors of tracer signal intensities. D/A is the D value divided by the A value, where D is the diffusion coefficient of the diffusion equation, and A is the emission coefficient of CSF efflux. "$(D/A)^*$" indicates the D/A value that minimized mean square errors (arrow). **d** CSF tracer signals in the mouse brain (left) and those calculated by our simulation (right). Signal intensities within the boxes were measured and plotted in (**e**). **e** Signal intensities of the CSF tracer in the mouse cortex (green) and those calculated by our simulations (purple). The relationship between signal intensities and the distance from the brain surface is shown. The term (arb. units) is abbreviated for arbitrary units. Scale bars, 2.5 mm (**a**) and 1 mm (**b**, **d**). Source data are provided as a Source Data file.

that our model well recapitulated the average distribution patterns of tracer signals (Fig. 1d, e). These results indicate that our model is appropriate for investigating glymphatic circulation in the brain.

The cerebral cortex leads to increased CSF exposure in cortical neurons

We next applied our model to the larger brains of monkeys and humans. We used images of monkey and human brains that are available online (monkey, http://brainmaps.org/index.php; human, http://brainmuseum.org/, https://doi.org/10.1038/s41597-019-0254-8 and https://doi.org/10.3389/fnana.2020.536838) (Supplementary Fig. 2). Interestingly, our simulations showed that the areas exhibiting efficient glymphatic circulation roughly corresponded to the gray matter of the cerebral hemispheres in both monkeys (Fig. 2a, b, green) and humans (Fig. 2e, f, green).

Although the cerebral cortex, a structure in the cerebral hemispheres comprising layered gray matter, is one of the most prominent features conserved in mammalian brains[31,32], its biological importance remains unclear. Our results raised the possibility that the cerebral cortex is a structure that facilitates the accumulation of cortical neurons close to the cortical surface so that a greater number of neurons can benefit from efficient glymphatic circulation. To test this possibility, we created imaginary monkey and human cerebral hemispheres possessing the same numbers of cortical neurons compared with real monkey and human cerebral hemispheres, but in which cortical neurons did not form gray matter and were evenly distributed throughout the hemispheres (Fig. 2a, e, lower panels, red). We then simulated CSF solute concentrations at cortical neurons using the $(D/A)^*$ value, and histograms showed, in both monkeys and humans, that more neurons in the hemispheres with a cerebral cortex benefitted from efficient glymphatic circulation (Fig. 2c, g, green) compared with the imaginary hemispheres in which neurons were evenly distributed throughout the cerebral hemisphere (Fig. 2c, g, purple). On average, neurons in hemispheres with a cerebral cortex were exposed to CSF solute concentrations that were almost 2 times higher than concentrations in those in which neurons were evenly distributed (Fig. 2d, h). These results indicate that many neurons in the cerebral cortex can benefit from efficient glymphatic circulation. It should be noted that the benefit to cortical neurons was 2.2 times higher in humans (Fig. 2h) but only 1.8 times higher in monkeys (Fig. 2d). This result suggests that the importance of the accumulation of neurons in the cerebral cortex is greater in larger brains.

The importance of cortical folds for efficient glymphatic circulation

During evolution, the number of neurons in the cerebral cortex has increased significantly[5]. There seemed two possible options for how the number of neurons in the cerebral cortex increased. The first option would be an increase in the thickness of the cerebral cortex without the formation of cortical folds. The second option involved the creation of cortical folds to increase the surface area of the cerebral cortex while preserving its thickness[31]. Because many mammals have cortical folds, it seems plausible that the folded cerebral cortex has advantages compared to the unfolded, thick cerebral cortex. However, the biological importance of cortical folds still remains unclear.

To examine whether the acquisition of cortical folds led to efficient glymphatic circulation, we created an imaginary human cerebral hemisphere which has the same number and density of cortical neurons but in an unfolded, thicker cerebral cortex (Fig. 3a, middle row). We then simulated patterns of glymphatic circulation using the $(D/A)^*$ value and analyzed CSF solute concentrations at cortical neurons (Fig. 3a, b, green). Histograms showed that more neurons benefited from efficient glymphatic circulation in the folded hemisphere (Fig. 3c, green) compared with the imaginary unfolded hemisphere with a thicker cerebral cortex (Fig. 3c, purple). The average CSF solute concentration at cortical neurons was 2.7-fold higher in the folded hemisphere compared with the unfolded hemisphere (Fig. 3d, 1st and 3rd from left). Consistent results were obtained using a monkey cerebral hemisphere (Supplementary Fig. 3a–d). These results indicate that cortical folds are important structures for enhancing glymphatic circulation in the cerebral cortex. It should be noted that the effects of cortical folds on glymphatic circulation were stronger in humans than in monkeys (Fig. 3d and Supplementary Fig. 3d) (human, 2.7-fold increase; monkey, 1.7-fold increase), suggesting that cortical folds are more important for enhancing glymphatic circulation in larger brains. Cortical folds increase the efficiency of glymphatic circulation around cortical neurons, presumably by both increasing the surface area of the cerebral hemispheres and reducing the thickness of the cerebral cortex.

To investigate the combinatorial effects of the cerebral cortex and cortical folds, we created an imaginary human cerebral hemisphere without cortical folds and without a cerebral cortex. In this hemisphere, the same number of neurons as found in a folded hemisphere were evenly distributed throughout (Fig. 3a, bottom row). The average values of CSF solute concentrations at cortical neurons showed that the cerebral cortex and cortical folds have synergistic effects on increasing the efficiency of glymphatic circulation (Fig. 3c, d). We examined increases of CSF solute concentrations resulting from the formation of the cerebral cortex and cortical folds and found that the increase was significantly larger when they were combined compared with the summation of the individual increase caused by each independently (increase caused by the combination of the cerebral cortex and cortical folds, 4.78 ± 0.6; increase caused by the cerebral cortex plus increase caused by cortical folds, 2.72 ± 0.3; $p < 0.01$, Student's t test). Although similar results were obtained using monkey cerebral hemispheres (Supplementary Fig. 3c, d), the synergistic effects were stronger in humans than in monkeys (Fig. 3d and Supplementary Fig. 3d) (human, 1.8-fold increase; monkey, 1.4-fold increase). These results indicate that, during evolution, the acquisition of the cerebral cortex and cortical folds together contributed to enhancing the efficiency of glymphatic circulation in the enlarged cerebral hemispheres of gyrencephalic brains.

The effects of cortical folds on glymphatic circulation in white matter of the cerebral hemispheres

The enlargement and folding of the cerebral hemispheres during evolution included the significant expansion of not only the cerebral cortex (i.e., gray matter) but also subcortical white matter[32]. Therefore, we next examined the effect of cortical folds on glymphatic circulation in white matter. We simulated glymphatic circulation in the imaginary human and monkey cerebral hemispheres with and without cortical folds described above.

Our data clearly showed that the average CSF solute concentrations in white matter were higher in the folded hemispheres compared with the unfolded hemispheres in both humans and monkeys (Fig. 3e and Supplementary Fig. 3e). In addition, the effects of cortical folding on overall glymphatic circulation throughout the entire cerebral hemisphere were also observed (Fig. 3f and Supplementary Fig. 3f). Taken together with the results for glymphatic circulation in gray matter, these findings indicate that cortical folds have positive effects on glymphatic circulation in both gray matter and white matter in the cerebral hemispheres.

In vivo CSF influx patterns into folded cerebral hemispheres

The cerebral hemispheres have markedly expanded during evolution, and CSF influx from the brain surface is presumed to be inefficient in the deep regions of enlarged cerebral hemispheres. Our simulation data in this study uncovered that cortical folds are an important development that enhanced glymphatic circulation, and we further hypothesized that an additional unknown feature enhances glymphatic circulation in the large folded cerebral hemispheres.

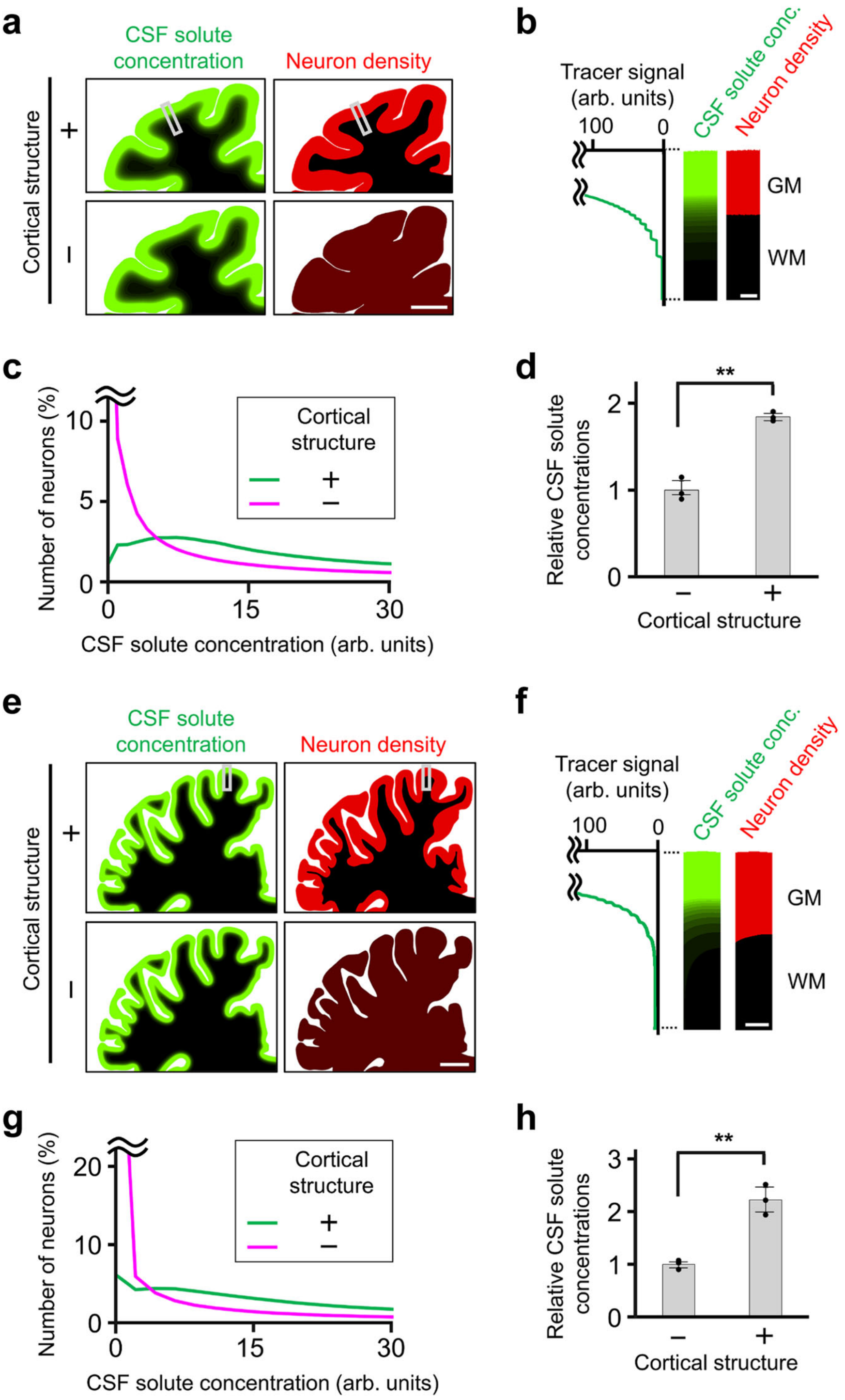

Fig. 2 | The cerebral cortex promotes efficient glymphatic circulation in cortical neurons. The distributions of CSF solutes in monkey (**a**–**d**) and human (**e**–**h**) cerebral hemispheres were modeled by our simulations. In addition to an imaginary hemisphere of the normal brain (cortical structure +), imaginary hemispheres without the cerebral cortex, in which neurons are evenly distributed throughout the hemispheres (cortical structure −), were also used. **a**, **e** Distributions of CSF solutes (green) and neurons (red) in the monkey hemisphere (**a**), and the human hemisphere (**e**). Images within the boxes in (**a**) and (**e**) were magnified and are shown in (**b**) and (**f**), respectively. **b**, **f** Magnified images of the distributions of CSF solutes (green) and neurons (red) around the cortical surface in the monkey hemisphere (**b**) and the human hemisphere (**f**). Tracer signal intensities are also shown. GM, gray matter; WM, white matter. **c**, **g** Histograms of CSF solute concentration at cortical neurons in the cerebral hemispheres with (green) and without a cortical structure (purple). Histograms from monkeys (**c**) and humans (**g**) are shown. **d**, **h** Quantifications of average CSF solute concentrations at cortical neurons in the cerebral hemispheres with and without a cortical structure. $p = 0.0020$ (**d**) and 0.0045 (**h**). The bars represent the average CSF solute concentration at cortical neurons in each type of hemisphere divided by the average solute concentration at cortical neurons in the hemisphere without a cortical structure. The term (arb. units) is abbreviated for arbitrary units. The graphs represent mean ± SD. $^{**}p < 0.01$, paired one-tailed Student's t test. $n = 3$ brains for each condition. The results from monkeys (**d**) and humans (**h**) are shown. Scale bars, 5 mm (**a**), 0.5 mm (**b**), 10 mm (**e**) and 1 mm (**f**). Source data are provided as a Source Data file.

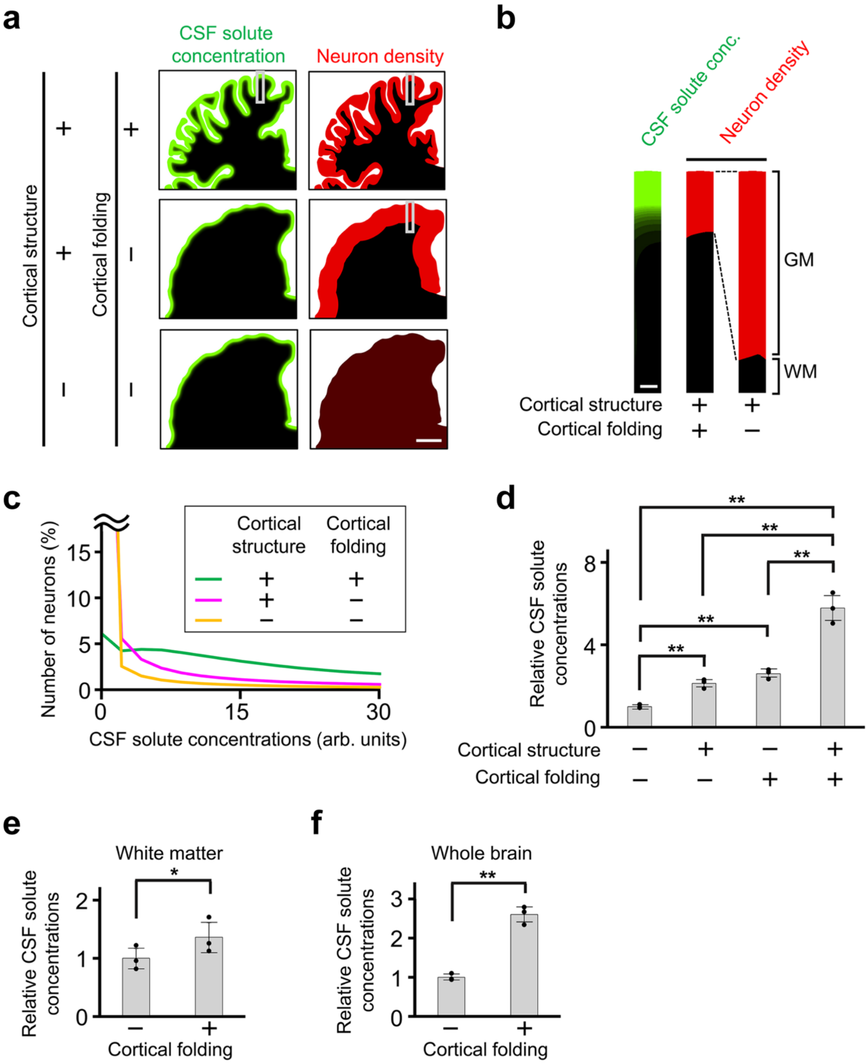

Fig. 3 | The importance of cortical folds for efficient glymphatic circulation in the human cerebral hemispheres. The distribution of CSF solutes in the human cerebral hemispheres was modeled by our simulations. In addition to an imaginary hemisphere of the normal brain (cortical structure +, cortical folding +), one without cortical folds (cortical structure +, cortical folding −) and one with neither cortical folds nor a cerebral cortex, in which neurons are evenly distributed throughout the hemisphere (cortical structure −, cortical folding −), were also used. **a** Distributions of CSF solutes (green) and neurons (red). Images within the boxes were magnified and are shown in (**b**). **b** Magnified images of the distributions of CSF solutes (green) and neurons (red) around the cortical surface. GM, gray matter; WM, white matter. **c** Histograms of CSF solute concentration at cortical neurons in the cerebral hemisphere of a normal brain (green), in one without cortical folds (purple), and in one with neither cortical folds nor a cerebral cortex (yellow). **d** Quantifications of average CSF solute concentrations at cortical neurons. The bars represent the average CSF solute concentration at cortical neurons in each type of hemisphere divided by the average solute concentration at cortical neurons in the hemisphere with neither folds nor a cortical structure. $p = 0.0037$ (CS−CF− vs. CS+CF−), 0.0031 (CS−CF− vs. CS−CF+), 0.0045 (CS−CF+ vs. CS+CF+), 0.0045 (CS+CF− vs. CS+CF+) and 0.0040 (CS−CF− vs. CS+CF+) (CS, cortical structure; CF, cortical folding). **e** Quantifications of average CSF solute concentrations in white matter. The bars represent the average CSF solute concentration in white matter in each type of hemisphere divided by the average solute concentration in the white matter of the hemisphere without cortical folds. $p = 0.033$. **f** Quantifications of average CSF solute concentrations in the entire hemisphere. $p = 0.0031$. The bars represent the overall average CSF solute concentration in each type of hemisphere divided by the overall average solute concentration in the hemisphere without cortical folds. The term (arb. units) is abbreviated for arbitrary units. The graphs represent mean ± SD. $^{*}p < 0.05$, $^{**}p < 0.01$, paired one-tailed Student's t test. $n = 3$ brains for each condition. Scale bars, 10 mm (**a**) and 1 mm (**b**). Source data are provided as a Source Data file.

To test this hypothesis, we utilized carnivore ferrets (*Mustela putorius furo*) because the cerebral hemispheres of ferrets have folds on their surface and are much larger than those of mice[10]. Ferrets have been widely used for investigating the molecular mechanisms underlying the folding and expansion of the cerebral hemispheres[10,18,20,33]. We injected the FITC-labeled dextran, a CSF tracer, into the cisterna magna of adult ferrets and mice. The brains were dissected 2 hours later and washed by gentle shaking for a few seconds to remove the CSF tracer remaining on the brain surface. We found an intriguing distribution pattern of tracer signals on the ferret cerebral hemispheres that was not observed on the mouse cerebral hemispheres (Fig. 4a). We found that tracer signals were markedly stronger at sulci than at gyri in the ferret cerebral hemispheres (Fig. 4a, b), raising the possibility that CSF influx into the cerebral hemispheres is more efficient at sulci than at gyri. Strong tracer signals were consistently observed at various sulci, including the cruciate sulcus, the coronal sulcus, the ansate sulcus, the lateral sulcus, the pseudosylvian sulcus, and the suprasylvian sulcus (Supplementary Fig. 4).

However, it remained possible that the efficiency of CSF influx is the same between sulci and gyri, and the strong tracer signals at sulci resulted from the summation of tracer signals along the deep grooves of sulci. To exclude this possibility, we prepared coronal sections of

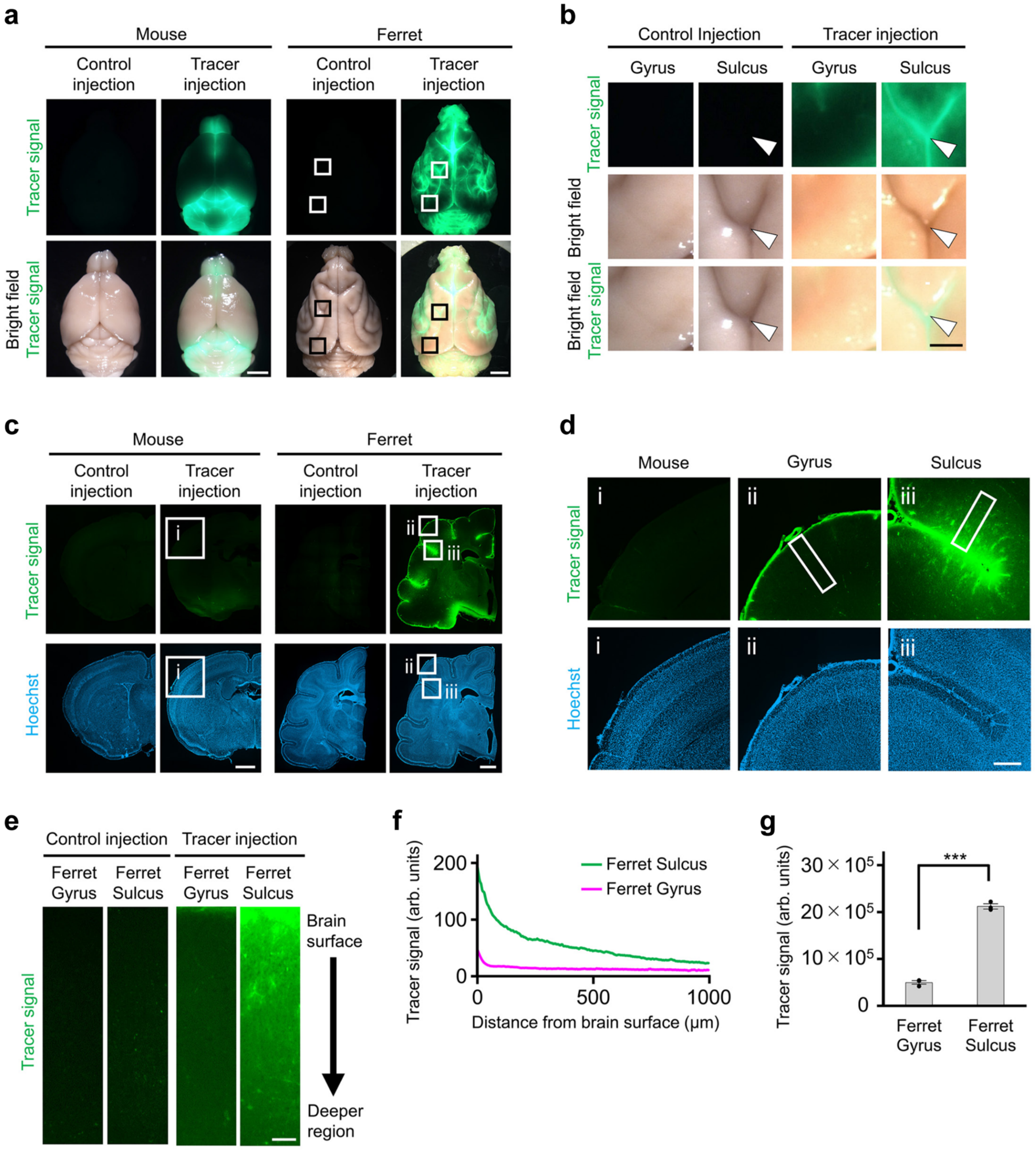

Fig. 4 | In vivo CSF influx patterns in the gyrencephalic ferret brain. a Mouse and ferret brains injected with or without a CSF tracer. Dorsal views are shown. 1-year-old mice and 3- to 4-year-old ferrets were used. The experiments were repeated at least 3 times independently and showed similar results. **b** Magnified images of the areas within boxes in (**a**). Arrowheads indicate the positions of sulci. **c** Coronal sections of mouse and ferret cerebral hemispheres. **d** Magnified images of the areas within boxes in (**c**). (ii) and (iii) correspond to the coronal gyrus and the suprasylvian sulcus, respectively, in the ferret cerebral hemisphere. Note that the CSF tracer signal intensity was greater in sulci than in gyri. **e** Higher magnification images around the brain surface from within the boxes in (**d**). Tracer signals are shown in columns extending inward from the brain surface. **f** Signal intensities of the CSF tracer in the ferret sulcus (green) and the ferret gyrus (purple). The relationship between signal intensity and the distance from the brain surface is shown. **g** Average intensities of tracer signals in the ferret sulcus and the ferret gyrus. $p = 0.000014$. The term (arb. units) is abbreviated for arbitrary units. The graph represents mean ± SD. $^{***}p < 0.001$, unpaired two-tailed Student's t test. $n = 3$ animals for each condition. Scale bars, 2.5 mm (**a**, mouse), 5 mm (**a**, ferret), 2 mm (**b**), 1 mm (**c**, mouse), 2 mm (**c**, ferret), 500 μm (**d**), and 100 μm (**e**). Source data are provided as a Source Data file.

the ferret cerebral hemispheres. Consistent with our macroscopic observation (Fig. 4a, b), we found that tracer signals were markedly and consistently stronger in sulcal regions than in gyral regions at various places (Fig. 4c, d and Supplementary Fig. 5). Tracer signals in superficial sulcal regions were stronger than in deep sulcal regions (Fig. 4e, f), suggesting that higher tracer signals in sulcal regions are derived from efficient CSF influx from the surface of the cerebral hemispheres. The average intensity of tracer signals was significantly higher in sulcal regions than in gyral regions (ferret sulcus, $21.2 \times 10^5 \pm 0.7 \times 10^5$; ferret gyrus, $5.0 \times 10^5 \pm 0.6 \times 10^5$; $^{***}p < 0.001$, Student's t test) (Fig. 4g). Because the efficiency of tracer injection could vary, we also measured the intensity of tracer signals in the cerebellum, and for normalization, the average intensities in the cerebral cortex were divided by those in the cerebellum. Even after this normalization, sulcal regions exhibited significantly stronger signals compared with gyral regions (Supplementary Fig. 6). Consistent results were obtained with isoflurane anesthesia and with isoflurane plus dexmedetomidine anesthesia (Supplementary Fig. 7a–c). Furthermore, consistent results were also observed in fresh-frozen sections made without perfusion fixation (Supplementary Fig. 7d–f).

These results clearly indicate that CSF enters into the ferret cerebral hemispheres more efficiently at sulci than at gyri. In contrast, the cerebral hemispheres of mice of different ages did not show such localized CSF influx (Fig. 4 and Supplementary Fig. 8). Our findings uncovered a unique feature of the folded ferret cerebral hemispheres related to the glymphatic system and may indicate that sulcus-dominant CSF influx enhances glymphatic circulation in the enlarged and folded cerebral hemispheres of gyrencephalic brains.

Distribution patterns of astrocytes and AQP4 expression in ferrets

Previous studies using mice reported that the CSF in the subarachnoid space flows into the parenchyma through astrocytic endfeet at the surface of the cerebral hemispheres[21,22]. Therefore, we compared the density of astrocytes in layer 1 between sulcal and gyral regions at multiple positions in the ferret cerebral hemispheres. We performed immunohistochemistry for glutamine synthetase (GS), which is an astrocyte marker, and counted the number of GS-positive cells in layer 1 (Fig. 5a, band Supplementary Fig. 9a). We found that the density of GS-positive cells in layer 1 was significantly higher in sulcal regions than in gyral regions (sulcus, 469 ± 63; gyrus, 233 ± 24; $^{**}p < 0.01$, Student's t test) (Fig. 5a, b). Consistent results were obtained using other astrocyte markers (S100β and GFAP) (Supplementary Figs. 9b, c and 10a–d). These results indicate that astrocytes are more abundant in sulcal regions than in gyral regions. In contrast, we did not find significant differences in the density of GS-positive astrocytes in layers 2-4 between gyri and sulci (Supplementary Fig. 10e, f).

AQP4 is a water channel preferentially distributed at astrocytic endfeet, and it has been shown using mice that AQP4 in astrocytes is crucial for CSF influx into the brain parenchyma[21–23]. Therefore, we next performed GS immunohistochemistry and *AQP4* in situ hybridization (Fig. 5c and Supplementary Fig. 11a) and counted the number of *AQP4*-positive astrocytes in layer 1 (Fig. 5d). The density of *AQP4*-positive astrocytes was significantly higher in sulcal regions than in gyral regions (sulcus, 365 ± 60; gyrus, 186 ± 58; $^{**}p < 0.01$, Student's t test) (Fig. 5d), suggesting that an increase in AQP4-positive astrocytes mediates sulcus-dominant CSF influx.

We also examined the expression levels of *AQP4* mRNA in astrocytes (Fig. 5e). The *AQP4* signal intensity in each GS-positive astrocyte in layer 1 was measured, and the average *AQP4* signal intensities were calculated. We found the expression levels of *AQP4* mRNA in astrocytes were significantly higher in sulcal regions than in gyral regions (sulcus, 44.7 ± 3.1; gyrus, 28.0 ± 4.3; $^{**}p < 0.01$, Student's t test) (Fig. 5f). This result indicates that AQP4 is more abundantly expressed in astrocytes in sulcal regions than in gyral regions. We then investigated the localization of AQP4 around blood vessels. We performed AQP4 immunostaining and measured the ratio of AQP4 signal intensities in astrocytic endfeet around blood vessels to those in the surrounding parenchyma. This ratio was significantly higher in sulcal regions than in gyral regions (sulcus, 5.31 ± 0.20; gyrus, 3.78 ± 0.13; $^{**}p < 0.01$, Student's t-test) (Fig. 5g, h and Supplementary Fig. 9d). Thus, our findings suggest that high AQP4 expression and AQP4 localization to astrocyte endfeet also contributes to efficient CSF influx in sulcal regions.

We also investigated vascular density and the size of the perivascular space in mice and ferrets. To investigate vascular density, we performed immunostaining for α-smooth muscle actin (SMA) and counted the number of SMA-positive arteries in layer 1 (Supplementary Figs. 9e and 12a, b). To measure the size of the perivascular space, we performed double immunostaining for GFAP and SMA and measured the size of the space between the GFAP-positive astrocytic endfeet and the SMA-positive vascular wall. Interestingly, within the ferret cerebrum, vascular density and the size of the perivascular space were significantly greater in sulcal regions than in gyral regions (Supplementary Fig. 12b, d). Vascular density may also be involved in sulcus-dominant CSF influx in ferrets.

We also compared the density of *AQP4*-positive astrocytes and the *AQP4* signal intensity in layer 1 of two additional areas in the ferret cerebral cortex (splenial sulcus vs posterior sigmoid gyrus, pseudosylvian sulcus vs anterior ectosylvian gyrus). Consistent with our data using the primary somatosensory cortex (Fig. 5), the density of *AQP4*-positive astrocytes and the *AQP4* signal intensity were significantly higher in sulcal regions than in gyral regions (Supplementary Fig. 13). These results may indicate that the distribution of astrocytes and the *AQP4* expression patterns we found are common features among various cortical areas.

AQP4 mediates sulcus-dominant CSF influx

To examine whether AQP4 indeed mediates sulcus-dominant CSF influx, we injected FITC-labeled dextran together with the AQP4 inhibitor TGN-020 into the cisterna magna of adult ferrets[25,34,35]. Our macroscopic observation revealed that tracer signals at sulci were markedly reduced by TGN-020 (Fig. 6a, b). Coronal sections also showed that tracer signals in sulcal regions were markedly reduced by TGN-020 (Fig. 6c–e). Our quantification showed that the reduction of tracer signals was more prominent in sulcal regions than in gyral regions (sulcus: control, $25.3 \times 10^5 \pm 2.9 \times 10^5$; TGN, $8.8 \times 10^5 \pm 3.2 \times 10^5$; $^{**}p < 0.01$, Student's t test) (gyrus: control, $5.8 \times 10^5 \pm 0.8 \times 10^5$; TGN, $2.4 \times 10^5 \pm 1.0 \times 10^5$; $^{*}p < 0.05$, Student's t test) (Fig. 6f, g). We then calculated the fold change in the reduction of tracer signals by TGN-020 and found that the reduction was more prominent in sulcal regions than in gyral regions (gyrus, 0.51 ± 0.03; sulcus, 0.32 ± 0.08; $^{*}p < 0.05$, Student's t test) (Fig. 6h). These results indicate that AQP4 plays an important role in sulcus-dominant CSF influx.

The effect of sulcus-dominant CSF influx on glymphatic circulation

To investigate the effect of sulcus-dominant CSF influx on glymphatic circulation, we made another mathematical model. In addition to D/A, we manually divided the ferret brain surface into the sulcal surface (Fig. 7a, green) and the gyral surface (Fig. 7a, purple) and defined c_s/c_g, which reflects the ratio of the CSF influx efficiency at the sulcal surface to that at the gyral surface (Fig. 7a). $c_s/c_g > 1.0$ indicates sulcus-dominant CSF influx, while $c_s/c_g = 1$ indicates uniform CSF influx without a distinction between gyri and sulci. We fitted the model to the measured tracer signal values in the ferret cerebral hemispheres using various D/A and c_s/c_g values (see Supplementary Method for details). We found that the mean square error of signal intensities was minimal when c_s/c_g was 3.5 (Fig. 7b, red box). Under these conditions, our simulation showed that the average distribution of tracer signals in the ferret brain was well recapitulated (Fig. 7c, d). These results suggest that CSF influx was 3.5 times higher in sulcal regions than in gyral regions of the ferret cerebral hemispheres.

To examine the biological importance of sulcus-dominant CSF influx, we simulated the patterns of CSF solute concentrations with various c_s/c_g values, including 3.5, which was obtained using the ferret brain (Fig. 7b), and 1.0, which represents a hypothetical condition with uniform CSF influx. We then compared these results under the condition that the total amount of CSF influx into the ferret cerebral hemispheres was the same in both cases. We found that the minimum value of CSF solute concentration in gray matter was higher when the c_s/c_g value was 3.5 compared to when the c_s/c_g value was 1.0 (Fig. 7e), suggesting that sulcus-dominant CSF influx contributes to raising the minimum CSF solute concentration in gray matter. Interestingly, our simulation showed that the minimum CSF solute concentration in gray matter was highest when the c_s/c_g value was 2.7 (Fig. 7e). Because the measured c_s/c_g value of 3.5 is close to the optimal c_s/c_g value of 2.7 (Fig. 7e), it seemed reasonable to speculate that sulcus-dominant CSF influx in vivo employs a c_s/c_g value resulting in glymphatic circulation close to the ideal state.

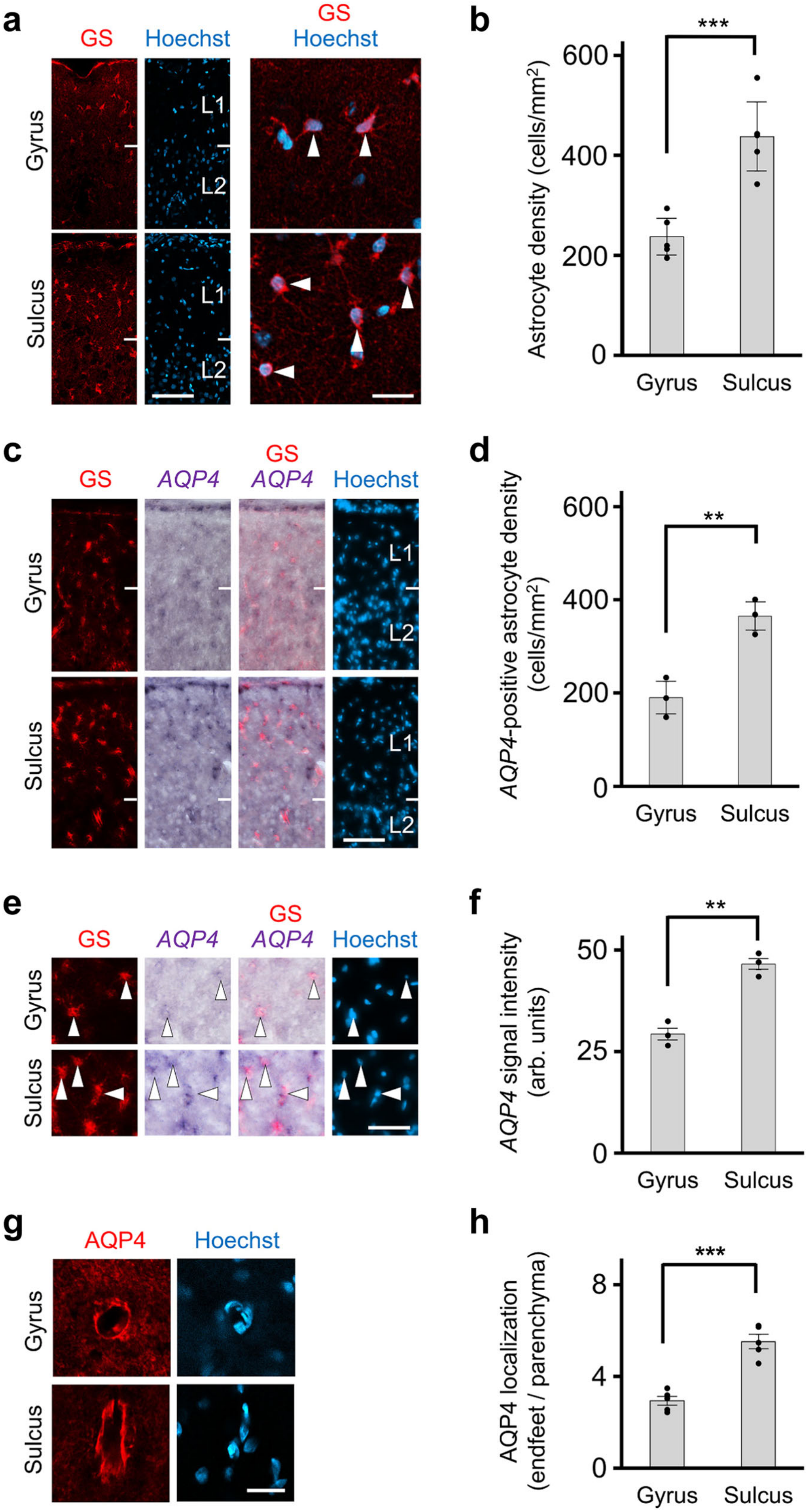

Distribution patterns of astrocytes and *AQP4* in the human cerebral cortex

We next examined the distribution patterns of astrocytes and AQP4 in layer 1 of the human cerebral cortex. Consistent with our finding in ferrets, GS immunohistochemistry showed that astrocytes were more abundant in sulcal regions than in gyral regions (Fig. 8a). Our quantification showed that the density of astrocytes in layer 1 was significantly higher in sulcal regions than in gyral regions (sulcus, 463 ± 23; gyrus, 199 ± 21; $^{**}p < 0.01$, Student's t-test) (Fig. 8b). Double staining with GS immunohistochemistry and *AQP4* in situ hybridization showed that the density of *AQP4*-positive astrocytes in layer 1 was significantly higher in sulcal regions than in gyral regions (sulcus,

Fig. 5 | The distribution patterns of astrocytes and AQP4 expression in the ferret cerebral cortex. Coronal sections corresponding to the primary somatosensory cortex of the ferret cerebral cortex were used. **a** Coronal section of the adult ferret brain stained with anti-glutamine synthetase (GS) antibody and Hoechst 33342. Superficial areas of the cerebral cortex corresponding to layers 1 and 2 are shown. High-magnification images in layer 1 are also shown on the right. Arrowheads indicate GS-positive astrocytes. **b** Quantification of the density of GS-positive cells in layer 1. $p = 0.00090$. **c** Coronal sections of the adult ferret brain were subjected to GS immunostaining, *AQP4* in situ hybridization, and Hoechst 33342 staining. Superficial areas of the cerebral cortex corresponding to layers 1 and 2 are shown. **d** Quantification of the density of *AQP4* and GS double-positive cells in layer 1. $p = 0.0068$. **e** High magnification images of astrocytes revealed with GS immunostaining, in situ hybridization for *AQP4* and Hoechst 33342 staining. Arrowheads indicate the *AQP4* and GS double-positive cells in layer 1. **f** Quantification of *AQP4* mRNA levels in layer 1 astrocytes. $p = 0.0020$. The average values of *AQP4*-signal intensities in GS-positive astrocytes in layer 1 are shown. **g** High magnification images of AQP4 immunostaining around blood vessels. **h** The ratio of AQP4 signal intensities in astrocytic endfeet around blood vessels to those in the surrounding parenchyma is shown. $p = 0.00011$. The term (arb. units) is abbreviated for arbitrary units. The graphs represent mean ± SD (**b**, **d**) and mean ± SEM (**f**, **h**). $^{**}p < 0.01$, $^{***}p < 0.001$, unpaired two-tailed Student's *t* test. $n = 5$ animals for (**b** and **h**), and $n = 3$ animals for (**d** and **f**). Numbers indicate layers in the cerebral cortex. Scale bars, 100 μm (**a**, left), 25 μm (**a**, right), 100 μm (**c**), 50 μm (**e**), and 20 μm (**g**). Source data are provided as a Source Data file.

413 ± 67; gyrus, 139 ± 33; $^{**}p < 0.01$, Student's *t* test) (Fig. 8c, d and Supplementary Fig. 11b). Furthermore, *AQP4* mRNA expression levels in astrocytes in layer 1 were significantly higher in sulcal regions than in gyral regions (sulcus, 38.4 ± 6.0; gyrus, 18.0 ± 0.9; $^{**}p < 0.01$, Student's *t* test) (Fig. 8e, f). These results are consistent with the data obtained using the ferret cerebral cortex. Although it is difficult to examine CSF influx patterns using FITC-labeled dextran in humans, it seems reasonable to speculate that sulcus-dominant CSF influx is also present in humans.

Discussion

Here we have established a mathematical model to simulate glymphatic circulation in the cerebral hemispheres. Our results showed that because cortical neurons accumulate close to the surface of the brain to form the cerebral cortex, cortical neurons can benefit from efficient glymphatic circulation. We also found that the efficiency of glymphatic circulation in both gray matter and white matter was markedly enhanced in the cerebral hemispheres with cortical folds. Furthermore, our in vivo study using ferrets uncovered sulcus-dominant CSF influx, which is mediated by AQP4 in sulcal regions. It seems plausible that an important factor determining the evolutionary trajectory of the cerebral hemispheres is the efficiency of the glymphatic circulation.

The biological importance of the cerebral cortex, cortical folds, and sulcus-dominant CSF influx

In the mammalian cerebral hemispheres, cortical neurons are accumulated close to the surface, forming the cerebral cortex[5,36]. Although it seems possible that neurons could be scattered throughout the cerebral hemispheres as they are in the diffuse nervous system, the cerebral cortex became a feature of the cerebral hemispheres of many mammals during evolution, suggesting that the cerebral cortex has some biological advantages compared with the diffuse nervous system. Similarly, as the number of cortical neurons has increased during evolution, cortical folds have become prominent on the surface of the cerebral cortex[31,37]. Although it seems possible to increase the number of cortical neurons by simply increasing the thickness of the cerebral cortex, most mammals employed cortical folds, suggesting that the folded cerebral cortex is advantageous compared to an unfolded, thick cerebral cortex. However, the biological roles of the cerebral cortex and cortical folds remain unclear. Here, we propose that both the cerebral cortex and cortical folds contribute to efficient glymphatic circulation in cortical neurons. In addition, we showed that sulcus-dominant CSF influx also leads to efficient glymphatic circulation in cortical neurons. Thus, our findings indicate that the cerebral cortex, cortical folds, and sulcus-dominant CSF influx synergistically cooperate to enhance the efficiency of glymphatic circulation in the mammalian cerebral hemispheres.

Our results showed that cortical folds also enhance glymphatic circulation in white matter. This result can be explained by two possible mechanisms. First, as shown in Fig. 3a, gray matter in the folded cerebral hemisphere (Fig. 3a, upper row, red) is thinner than that in an imaginary cerebral hemisphere having the same number and density of cortical neurons but whose surface does not have folds (Fig. 3a, middle row, red). As a result, the distance from the brain surface to white matter is shorter in the folded cerebral hemisphere, and this seems to be a reason why glymphatic circulation in white matter is better in the folded cerebral hemisphere. Second, because the surface area of the folded cerebral hemisphere is larger than that of the unfolded cerebral hemisphere, CSF can flow into the parenchyma from a broader surface area. Multiple mechanisms seem to cooperate to improve glymphatic circulation in the folded cerebral hemisphere.

During mammalian evolution, the cerebral hemispheres have markedly expanded[31,32,37]. This increase in the size of the cerebral hemispheres would presumably have a negative impact on the efficiency of glymphatic circulation in deep regions of the cerebral hemispheres. Interestingly, the large cerebral hemispheres of humans, monkeys, and ferrets are covered with many cortical folds, which are absent from the small cerebral hemispheres of mice[10,31]. Furthermore, among the cerebral hemispheres of various mammals, the larger cerebral hemispheres tend to have more cortical folds[10]. Thus, it seems plausible that cortical folds and sulcus-dominant CSF influx were adaptations that compensated for insufficient glymphatic circulation in enlarged cerebral hemispheres. Our findings propose a biological importance of cortical folds and may indicate that the evolutionary changes seen in the mammalian brain were at least partially driven by selection for efficient glymphatic circulation.

It is worth mentioning that tracer signals in the ventral side of the ferret brain, which corresponds to the hypothalamus, were strong (Fig. 4c), suggesting efficient glymphatic circulation in the hypothalamus. In addition to the cerebral hemispheres, it would be intriguing to investigate the biological importance of and the mechanisms underlying efficient glymphatic circulation in the hypothalamus in future experiments.

Sulcus-dominant CSF influx in folded cerebral hemispheres

In this study, we uncovered that CSF influx is markedly enhanced in sulcal regions of the ferret cerebral hemispheres. Because the sulcus is located deep in the cerebral hemisphere, it seems likely that enhanced CSF influx in sulcal regions contributes to efficient glymphatic circulation in the enlarged cerebral hemispheres of gyrencephalic brains. Consistent with this idea, our mathematical modeling demonstrated that increased CSF influx in sulcal regions markedly increased the efficiency of the glymphatic circulation.

We have shown that AQP4-positive astrocytes are accumulated in sulcal regions and that AQP4 mediates sulcus-dominant CSF influx in the ferret cerebral cortex. Importantly, we also found a similar accumulation of AQP4-positive astrocytes in sulcal regions in the human cerebral cortex. Therefore, it seems reasonable to speculate that sulcus-dominant CSF influx is also present in the human cerebral hemispheres, although it is difficult to directly examine CSF influx in the human brain using FITC-labeled dextran. A recent pioneering work also reported that CSF influx was more efficient in sulcal regions than in gyral regions of the pig brain[38]. Taken together with our findings, it

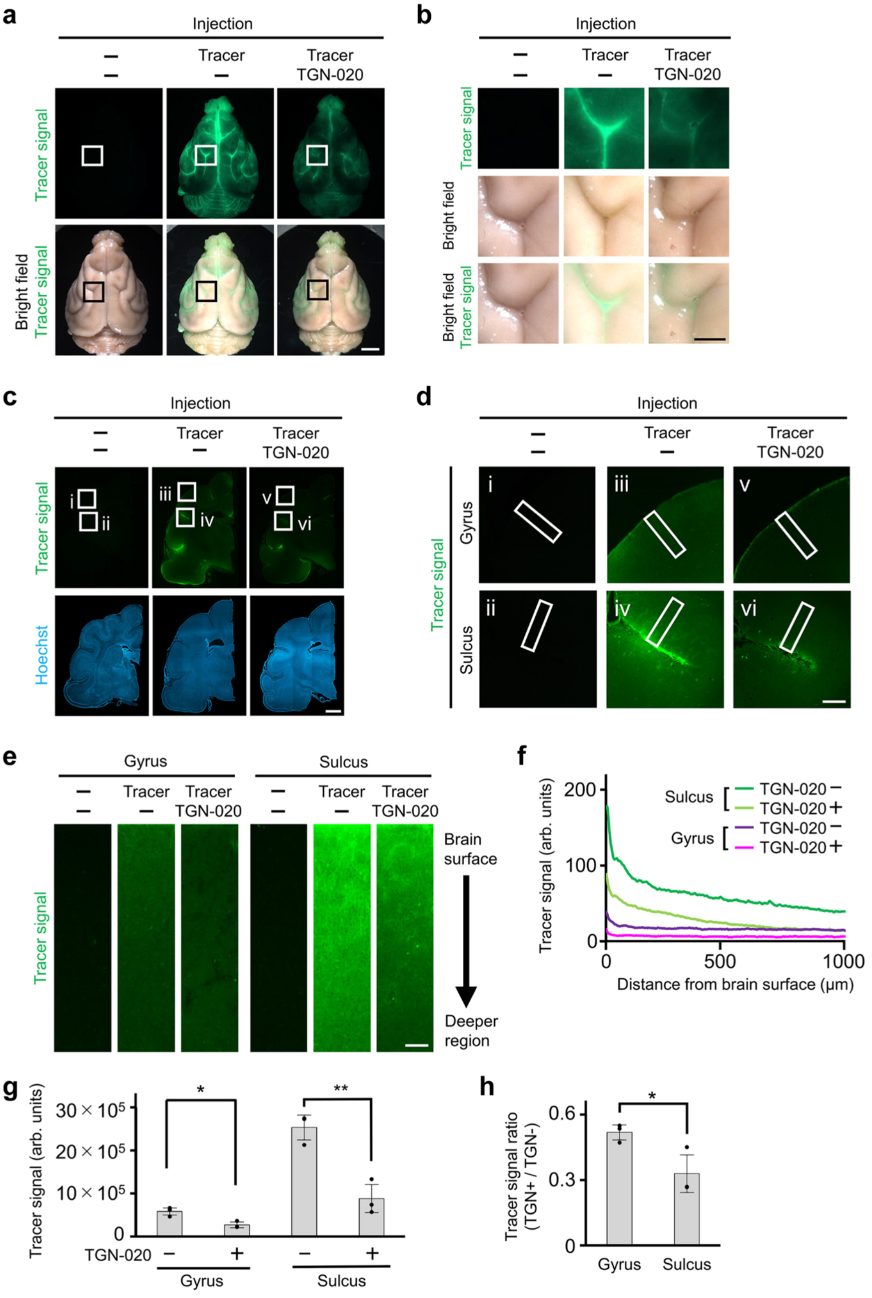

Fig. 6 | AQP4 mediates sulcus-dominant CSF influx in the ferret brain. **a** Ferret brain injected with the CSF tracer and TGN-020. Dorsal views are shown. The experiments were repeated at least 3 times independently and showed similar results. **b** Magnified images of the areas within boxes in (**a**). **c** Coronal sections of the ferret cerebral hemisphere. **d** Higher magnification images from within the boxes in (**c**). **e** High magnification images around the brain surface from within the boxes in (**d**). Tracer signals are shown in columns extending inward from the brain surface. **f** Signal intensities of the CSF tracer in ferret sulci and ferret gyri treated with or without TGN-020. The relationship between signal intensities and the distance from the brain surface is shown. **g** Average intensities of tracer signals in the ferret sulcus and the ferret gyrus treated with or without TGN-020. $p = 0.020$ (gyrus) and 0.0040 (sulcus). **h** The ratios of tracer signals in TGN-020-treated brain regions to those in TGN-020-untreated brain regions. The values shown in (**g**) were used for calculation. $p = 0.044$. The term (arb. units) is abbreviated for arbitrary units. The graphs represent mean ± SD. $^*p < 0.05$, $^{**}p < 0.01$, unpaired two-tailed Student's *t* test. $n = 3$ animals for each condition. Scale bars, 5 mm (**a**), 2 mm (**b**, **c**), 500 μm (**d**) and 100 μm (**e**). Source data are provided as a Source Data file.

seems likely that sulcus-dominant CSF influx is a conserved feature of the folded cerebral hemispheres of various mammals.

We previously reported that increased astrogenesis in white matter is crucial for the formation of cortical folds on the ferret cerebral hemisphere during development[20]. We also found that this increase in astrocytes is mediated by a positive feedback loop of fibroblast growth factor (FGF) signaling. In this study, we have shown that astrocytes in layer 1 are more abundant in sulcal regions than in gyral regions, and it seems plausible that a positive feedback loop of FGF signaling is also involved in the increase in astrocytes in sulcal regions. It would be intriguing to investigate the molecular mechanisms responsible for this increase.

It would be also interesting to examine the relationship between sulcus-dominant CSF influx and cortical folding. It seems possible sulcus-dominant CSF influx contributes to the formation of cortical folds. Conversely, it seems also plausible that cortical folds lead to the accumulation of astrocytes in sulcal regions via unknown mechanisms. To obtain insights into the relationship between sulcus-dominant CSF

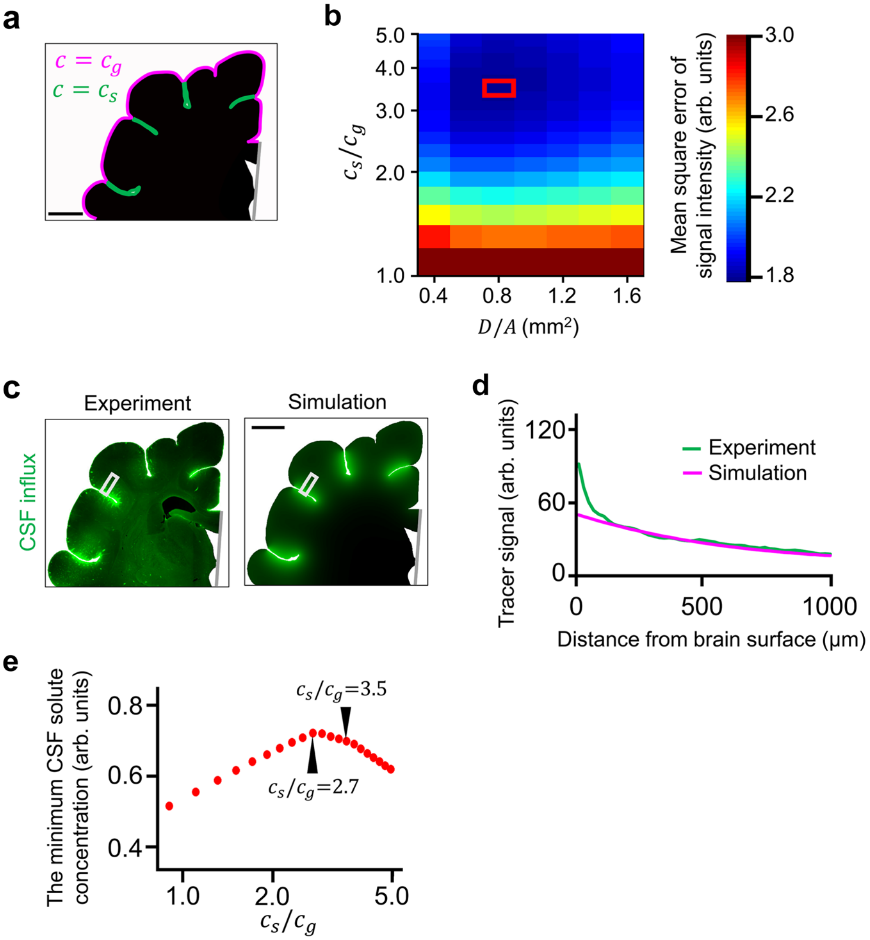

Fig. 7 | The effect of sulcus-dominant CSF influx on glymphatic circulation. a An illustration of a coronal section of a ferret cerebral hemisphere. We divided the brain surface into the sulcal surface (green) and the gyral surface (purple). The gray line indicates the midline where the hemisphere is connected to the other hemisphere. Therefore, we assumed that CSF does not flow into the parenchyma from the gray line. CSF influx efficiencies at sulci and gyri are written as c_s and c_g, respectively. **b** A heatmap showing the D/A value and the c_s/c_g value that minimized the mean square error of the signal intensity. Red and blue indicate large and small mean square errors, respectively. The combination of D/A and c_s/c_g that minimized the mean square error of the signal intensity is indicated by a red box. **c** CSF tracer signals in the ferret brain (left) and those calculated by our simulation procedure (right). Signal intensities within the boxes were measured and plotted in (**d**). **d** Signal intensities of the CSF tracer in the ferret cortex (green) and those calculated using our simulation procedure (purple). The relationship between signal intensities and the distance from the brain surface is shown. **e** Calculation of minimum CSF solute concentrations in gray matter depending on various c_s/c_g values. $c_s/c_g = 1$ means that CSF influx efficiencies at gyri and sulci are the same (i). When c_s/c_g was 2.7, the minimum CSF solute concentration was largest (ii). Our heatmap (**b**) showed that c_s/c_g in the ferret cerebral hemisphere was 3.5 (iii), which is close to the optimal c_s/c_g value of 2.7. The term (arb. units) is abbreviated for arbitrary units. $n = 3$ animals for the calculation of minimum CSF solute concentrations in gray matter. Scale bars, 2 mm (**a**, **c**). Source data are provided as a Source Data file.

influx and cortical folding, an investigation of the developmental time courses of sulcus-dominant CSF influx and cortical folding would be helpful. Experiments using developing ferrets would be important for obtaining a complete picture of the mechanisms leading to sulcus-dominant CSF influx and cortical folding.

Possible pathological involvement of glymphatic circulation

Previous studies demonstrated that the glymphatic system is crucial for the clearance of waste in the cerebral hemispheres and is involved in the pathogenesis of Alzheimer's disease[22,25,26]. Mammals with large cerebral hemispheres tend to live longer[39], and it is likely that the clearance of waste is more important in animals with long lives to prevent the deposition of waste. Therefore, it seems plausible that the increased efficiency of glymphatic circulation facilitated by cortical folds and sulcus-dominant CSF influx reduces the risk of various diseases, such as Alzheimer's disease, caused by the deposition of waste, especially in mammals with long life spans.

Human lissencephaly is often caused by defects in the radial migration of cortical neurons during development, and individuals with lissencephaly exhibit severe intellectual disability[12–16]. One possible reason why the mislocation of cortical neurons results in severe intellectual disability, even though the number of cortical neurons is relatively preserved, is that cortical circuits become miswired[31]. Our findings raised the possibility that insufficient glymphatic circulation around cortical neurons is also involved in severe intellectual disability. As our mathematical modeling has shown, when cortical neurons are distributed far from the cortical surface, glymphatic circulation in neurons becomes inefficient. Furthermore, because lissencephalic brains do not have cortical folds, the surface area of lissencephalic cerebral hemispheres is smaller than that of folded cerebral hemispheres, and as a result, glymphatic circulation itself should be inefficient in lissencephalic brains. It would be intriguing to investigate whether enhancement of glymphatic circulation could improve symptoms in lissencephalic patients.

Limitations and future perspectives for our modeling of glymphatic circulation

Our modeling included both diffusion and advection via perivascular spaces and approximated them together as macroscopic simple diffusion. It should be noted that because of this simplification, both the

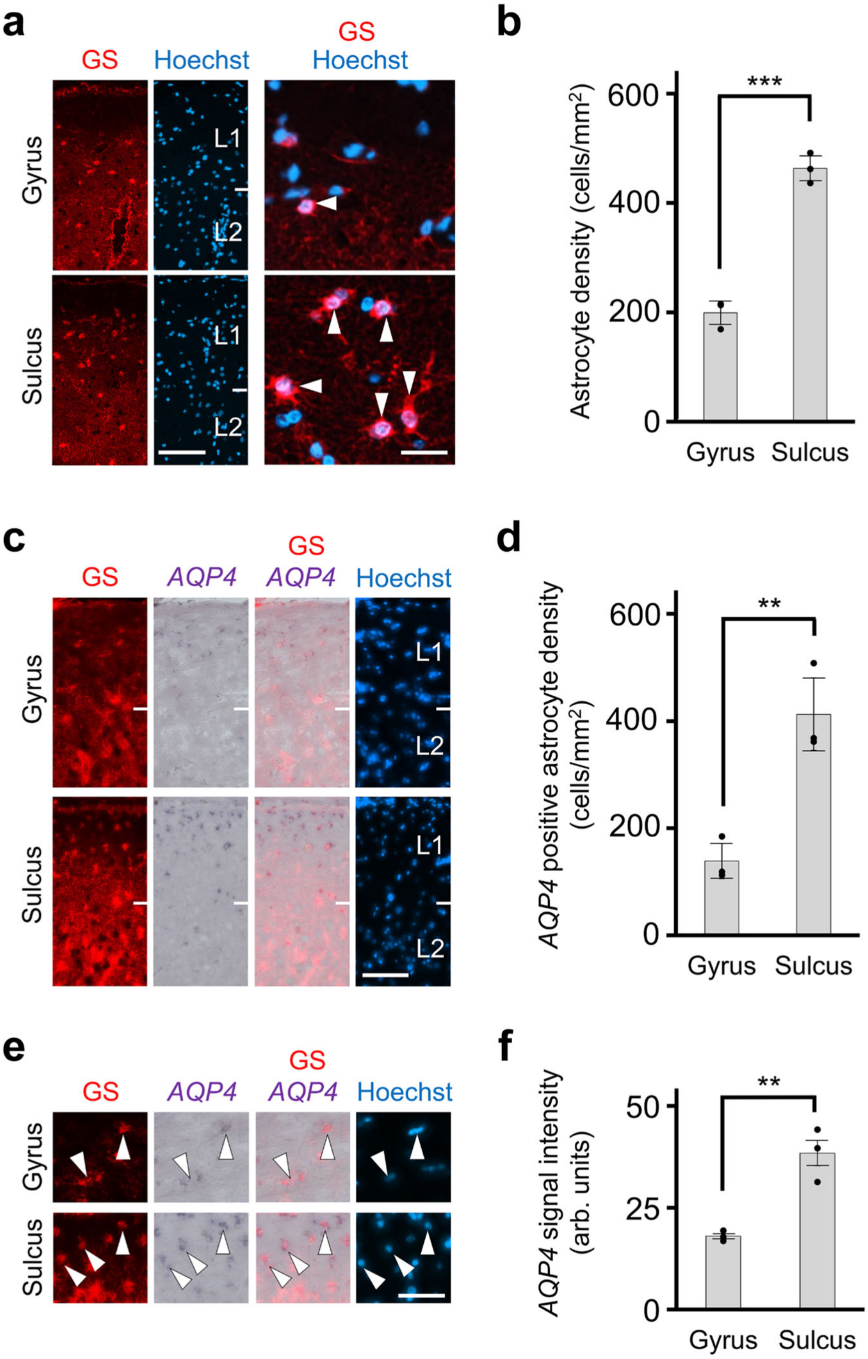

Fig. 8 | The distribution patterns of astrocytes and AQP4 expression in the human cerebral cortex. **a** Sections of the adult human brain stained with anti-GS antibody and Hoechst 33342. Superficial areas of the cerebral cortex corresponding to layers 1 and 2 are shown. High-magnification images from layer 1 are also shown on the right. Arrowheads indicate GS-positive astrocytes. **b** Quantification of the density of GS-positive cells in layer 1. $p = 0.00027$. **c** Sections of the adult human brain were subjected to GS immunostaining, *AQP4* in situ hybridization, and Hoechst 33342 staining. Superficial areas of the cerebral cortex corresponding to layers 1 and 2 are shown. **d** Quantification of the density of *AQP4* and GS double-positive cells in layer 1. $p = 0.0066$. **e** High magnification images of astrocytes revealed with GS immunostaining, in situ hybridization for *AQP4* and Hoechst 33342 staining. Arrowheads indicate the *AQP4* and GS double-positive cells in layer 1. **f** Quantification of *AQP4* mRNA levels in layer 1 astrocytes. $p = 0.0061$. The average values of *AQP4* signal intensities in GS-positive astrocytes in layer 1 are shown. The term (arb. units) is abbreviated for arbitrary units. The graphs represent mean ± SD (**b**, **d**) and mean ± SEM (**f**). $^{**}p < 0.01$, $^{***}p < 0.001$, unpaired two-tailed Student's *t* test. $n = 3$ animals for each condition. Numbers indicate layers in the cerebral cortex. Scale bars, 100 μm (**a**, left), 25 μm (**a**, right), 100 μm (**c**) and 50 μm (**e**). Source data are provided as a Source Data file.

diffusion coefficient D and the emission coefficient A in our model represented effective parameters. Specifically, D accounted for both molecular diffusion and advection via perivascular spaces. Even with this simplification, our modeling well recapitulated the macroscopic experimental distribution of tracer signals in the brain. However, it would be interesting to distinguish the functional contributions of diffusion and advection in glymphatic circulation at microscopic levels.

To simulate the distribution of CSF solutes in monkey and human cerebral hemispheres, $(D/A)^*$ and γ^*, which were calculated using the mouse cerebral hemispheres, were used in this study. As a next step, it would be desirable to use $(D/A)^*$ and γ^* calculated using monkey and human brains, though some of the necessary experiments pose significant challenges. Knowing the physical parameters of monkey and human brains would provide a more quantitative understanding of the variations in glymphatic circulation across animal species.

It also should be noted that our modeling and simulations were carried out in two dimensions. While our modeling and simulations basically succeeded in capturing the CSF solute distributions in the brain, it seemed possible that the reduction into two dimensions led to quantitative differences in the estimated distribution of CSF solutes. In future experiments, it would be important to expand our modeling and simulations to include three-dimensional analyses in order to improve the accuracy.

Methods

Ethics statement

All animal experiments were performed in accordance with protocols approved by the Animal Care Committee of Kanazawa University (AP21-035 and AP21-036). The experiments using human samples were performed in accordance with the guidelines of the Internal Review Board of Kanazawa University and a protocol approved by the Medical Ethics Committee of Kanazawa University (No. 3402).

Animals

Normally pigmented sable female ferrets (*Mustela putorius furo*) were purchased from Marshall Farms (North Rose, NY). Ferrets were maintained as described previously[40]. Ferrets were reared on a normal 16/8 hr light/dark schedule with free access to water and food at a room temperature of 20–22 °C and a humidity of 45–65%. ICR female mice were purchased from SLC (Hamamatsu, Japan). Mice were reared on a normal 12/12 hr light/dark schedule with free access to water and food at a room temperature of 20–26 °C and a humidity of 45–65%. Anesthesia was induced using 3-4% isoflurane and maintained using 2–2.5% isoflurane. Isoflurane alone was used unless otherwise mentioned.

To analyze the CSF influx pattern under an additional anesthetic condition, a combination of isoflurane and dexmedetomidine was used[41]. Anesthesia was induced using 3-4% isoflurane and two intraperitoneal injections of dexmedetomidine (0.015 mg/kg) and then maintained using 2–2.5% isoflurane[41]. Additional intraperitoneal injections of dexmedetomidine (0.015 mg/kg) were performed before and 1 h after tracer injection.

Human brain samples

After informed consent was obtained, human brain tissue samples were obtained from patients aged 61–75 years of both sexes with glioma. Noncancerous brain tissues were used.

Cisternal injection of the CSF tracer

Artificial CSF (aCSF) was made as described previously[42]. The CSF tracer FITC-conjugated lysine-fixable 3 kDa dextran (Thermo Fisher Scientific, D3306) was dissolved in aCSF at a concentration of 0.5%[22,24,42]. For the control injection, aCSF without a CSF tracer was used.

For the mathematical modeling, the CSF tracer was injected into the cisterna magna of 1-month-old mice using a Hamilton syringe. The CSF tracer was injected for 6.5 min with 2 μl/min. After the injection, the mice were kept in a supine position and fixed with 4% paraformaldehyde (PFA) 2 h later.

For the comparison between mice and ferrets, the CSF tracer was injected into the cisterna magna of 8-month-old mice, 1-year-old mice, and 3-4-year-old ferrets, which are almost comparable in terms of their developmental stage. 13 μl and 150 μl of the CSF tracer were injected into the cisterna magna of adult mice and adult ferrets, respectively. These volumes of the CSF tracer were determined according to the weights of the mouse brain and the ferret brain. Two hours after the injections, the animals were perfused with 4% PFA. The volume of the CSF tracer can also be determined according to the volume of the CSF in mice and ferrets, and in this case, the volume of the CSF tracer for ferrets would be larger (164 μl) than the amount we used (150 μl). It should be noted that even though we injected a smaller amount (i.e., 150 μl) of the CSF tracer, tracer signals were still markedly higher in ferret gyral regions than in the mouse cortex.

Cisternal injection of the AQP4 inhibitor

The AQP4 inhibitor TGN-020 (R&D Systems, 5425/10) was dissolved in dimethyl sulfoxide (DMSO) and then diluted with a CSF. The mixture of 0.4 μg/μl TGN-020 and 0.5% CSF tracer was injected into the cisternal magna for 6.5 min at a rate of 2 μl/min. The concentration of TGN-020 was determined based on a previous report[43]. Perfusion fixation was performed with 4% PFA/PBS 4 h later.

Preparation of tissue sections

Tissue sections were prepared as described previously[44,45]. Mice and ferrets were deeply anesthetized with 2–2.5% isoflurane and transcardially perfused with 4% PFA/PBS. Brains were dissected and post-fixed with 4% PFA/PBS. The brains were then cryoprotected with 30% sucrose/PBS for 5 days and embedded in an OCT compound. Coronal sections of 20 μm and 50 μm thicknesses were made using a cryostat. To obtain sections from unfixed fresh-frozen tissues, brains were dissected without perfusion fixation, embedded in an OCT compound, and frozen immediately. Coronal sections of 100 μm thickness were made using a cryostat and were treated with 4% PFA.

Immunohistochemistry

Immunohistochemistry was performed as described previously with slight modifications[46–48]. Coronal sections were permeabilized with 0.3% Triton X-100/PBS, incubated overnight with primary antibodies in 2% bovine serum albumin (BSA)/PBS, and washed with 0.3% Triton X-100/PBS three times for 5 min each. The sections were then incubated with secondary antibodies and Hoechst 33342 in 2% BSA/PBS for 2 h and washed with 0.3% Triton X-100/PBS three times for 5 min each. The sections were mounted on glass slides with Mowiol (Sigma-Aldrich). Anti-glutamine synthetase (GS) antibody (Sigma-Aldrich, Cat#G2781, Lot#064M4817V, 1:1000), anti-S100β antibody (Synaptic Systems, Cat#287003, Lot#1-6, 1:600), anti-glial fibrillary acidic protein (GFAP) antibody (Sigma-Aldrich, Cat#ab23345, Lot#GR234490-1, 1:500), anti-aquaporin 4 (AQP4) antibody (Millipore, Cat#3594, Lot#3286087, 1:500), anti-alpha smooth muscle actin (SMA) antibody (abcam, Cat#ab5694, Lot#3613002, 1:500), Alexa Fluor 647-conjugated donkey anti-mouse IgG antibody (Molecular Probe, Cat#31571, Lot#2420695, 1:500) and Cy3-conjugated donkey anti-rabbit IgG antibody (Jackson Immuno Research, Cat#711-165-152, Lot#139288, 1:500) were used.

In situ hybridization

In situ hybridization using digoxigenin-labeled RNA probes was performed as described previously with slight modifications[49,50]. Briefly, coronal sections of 20 μm thickness were incubated with digoxigenin-labeled RNA probes in hybridization buffer (50% formamide, 5 × saline sodium citrate buffer, 5 × Denhardt's solution, 0.3 mg/ml yeast RNA, 0.1 mg/ml herring sperm DNA, and 1 mM dithiothreitol). The sections were then incubated with an alkaline phosphatase-conjugated anti-digoxigenin antibody (Roche) and were visualized using nitro blue tetrazolium/bromochloroindolyl phosphate (NBT/BCIP) as substrates. The sections were then subjected to Hoechst 33342 staining. The AQP4 probe was described previously[51].

Microscopy

Epifluorescence microscopy was performed with BZ-9000 and BZ-X710 microscopes (Keyence) and an Axioimager Z2 (ZEISS). Confocal microscopy was performed with an LSM 900 (ZEISS).

Quantification of CSF tracer signals

Quantification of CSF tracer signals in tissue sections was performed with ImageJ software. Regions of interest (ROIs) with 250 μm width and 1000 μm length were selected in the cortex. The signal intensities of the CSF tracer at various depths from the brain surface were measured, and average signal intensities were plotted using the "Plot Profile" tool of ImageJ. Summation of CSF tracer signals in ROIs was measured using the "RawIntDen" tool of ImageJ. To remove background signals, the signal intensities of control samples were subtracted with the "Subtract" tool of ImageJ.

Quantifications of cell density and *AQP4* expression levels

Coronal sections were subjected to immunohistochemistry for GS, S100β, and GFAP; in situ hybridization for *AQP4*; and Hoechst 33342 staining.

To quantify the cell density of astrocytes in layer 1 and layers 2–4, the numbers of GS-positive astrocytes and S100β-positive astrocytes were manually counted using the "Cell counter" tool of ImageJ. To quantify the GFAP-positive area, the GFAP-positive area in layer 1 was measured using the "Measure" tool of ImageJ and then divided by the total area of layer 1 for normalization. To quantify the cell density of *AQP4*-positive astrocytes in layer 1, the number of GS- and *AQP4*-double positive cells was counted using the "Cell counter" tool of ImageJ. The areas of layer 1 and layer 2–4 were measured using the "Measure" tool of ImageJ. The cell density was calculated by dividing the number of astrocytes by the area.

To examine the expression levels of *AQP4* in astrocytes in layer 1, tissue background signals were subtracted. The mean intensities of *AQP4* signals in each GS-positive astrocyte in layer 1 were measured using the "Measure" tool of ImageJ, and the average *AQP4* signal intensities in GS-positive astrocytes were calculated.

Quantification of AQP4 localization

To quantify the localization of AQP4 in astrocytic endfeet, coronal sections were subjected to immunohistochemistry for AQP4 and Hoechst 33342 staining. Blood vessels with diameters larger than 10 μm were selected, and AQP4 signals, including those in the surrounding brain parenchyma, were measured using the "line plot" tool of ImageJ[24]. The ratio of the average of AQP4 signal intensities in vessels to those in the surrounding brain parenchyma was calculated.

Quantification of vascular density and the size of the perivascular space

Coronal sections were subjected to Hoechst 33342 staining and immunohistochemistry for SMA and GFAP. To quantify vascular density in ferret and mouse brains, the number of SMA-positive vessels with diameters larger than 10 μm in layer 1 was manually counted, and vascular density was calculated by dividing the number of vessels by the area[52]. To quantify the size of the perivascular space (PVS), the area between the inner circumference of GFAP-positive endfeet and the outer circumference of SMA-positive vessels was measured and then divided by the area within SMA-positive vessels for normalization[53].

Statistics

Student's *t*-test was used to determine statistical significance. Values in graphs represent mean ± SD or mean ± SEM.

Mathematical modeling and simulation procedures

Mathematical modeling of the glymphatic circulation. To develop a mathematical model of glymphatic circulation, we employed two main approximations. First, our model approximates CSF influx into the parenchyma from the subarachnoid space via perivascular spaces as uniform diffusion. Second, the model reduces the diffusion field to two dimensions in brain sections. When positions within sections were described as $\boldsymbol{x} = (x, y)$, and the concentration of CSF solutes at position $\boldsymbol{x}$ at time t was described as $c(\boldsymbol{x}, t)$, the following equation can be made:

$$\frac{\partial c(\boldsymbol{x},t)}{\partial t} = D\frac{\partial^2 c(\boldsymbol{x},t)}{\partial \boldsymbol{x}^2} - Ac(\boldsymbol{x},t). \tag{1}$$

The left side of the equation indicates the time differentiation of the CSF solute concentration. On the right side, the first and second terms represent diffusion and emission, respectively. D and A are diffusion and emission coefficients, respectively. We assumed that CSF influx from the brain surface into the parenchyma is uniform across its surface.

When the brain surface was written as φ_0 and the CSF solute concentration at φ_0 was described as c_0, the fixed boundary condition was applied:

$$c(\boldsymbol{x},t)|_{\boldsymbol{x}\in\varphi_0} = c_0. \tag{2}$$

When images of brain tissues were truncated at the midline φ_{m}, the mirror boundary condition was applied:

$$\frac{\partial c(\boldsymbol{x},t)}{\partial \boldsymbol{x}} \cdot \boldsymbol{n}(\boldsymbol{x})|_{\boldsymbol{x}\in\varphi_{\mathrm{m}}} = 0. \tag{3}$$

In Eq. (3), n($\boldsymbol{x}$) is the normal vector of the brain surface at position $\boldsymbol{x}$. Assuming that the glymphatic circulation in the cerebral hemispheres is under a steady state, the distribution of the CSF in the parenchyma can be calculated as a steady-state solution of Eqs. (1), (2), and (3).

Non-dimensionalization and numerical simulations. When the units of length, time, and concentration used $(D/A)^{\frac{1}{2}}, 1/A$, and c_0, respectively, Eqs. (1), (2), and (3) can be rewritten as follows:

$$\frac{\partial \bar{c}(\bar{\boldsymbol{x}},\bar{t})}{\partial \bar{t}} = \left(\frac{\partial^2 \bar{c}(\bar{\boldsymbol{x}},\bar{t})}{\partial \bar{\boldsymbol{x}}^2}\right) - \bar{c}(\bar{\boldsymbol{x}},\bar{t}), \tag{4}$$

$$\bar{c}(\bar{\boldsymbol{x}},\bar{t})|_{\bar{\boldsymbol{x}}\in\varphi_0} = 1. \tag{5}$$

$$\frac{\partial \bar{c}(\bar{\boldsymbol{x}},\bar{t})}{\partial \bar{\boldsymbol{x}}} \cdot \boldsymbol{n}(\bar{\boldsymbol{x}})|_{\bar{\boldsymbol{x}}\in\varphi_m} = 0. \tag{6}$$

Dimensionless constants and variables were expressed with overlines. Because we focused on the distribution of CSF solutes at a steady-state, the distribution of CSF solutes is independent of the time-related parameter $1/A$. Thus, among three units written above, a parameter for determining steady-state CSF solute concentrations was D/A.

We conducted numerical simulations for Eqs. (1), (2), and (3) by developing custom C + + software. Equation (1) was solved in the two-dimensional space discretized by a rectangular grid. The outline of the brain surface was manually extracted from images, and the brain surface φ_0, the midline boundary φ_{m}, and the brain parenchymal region were determined. Specifically, we used entire coronal sections for mouse, monkey, and human brains and halves of coronal sections for ferrets. The representative regions used for mathematical analyses in each brain section are shown in Supplementary Fig. 14.

The initial condition was given as the situation in which there were no CSF solutes in the brain parenchyma as described below:

$$c(\boldsymbol{x},t)|_{t=0} = 0. \tag{7}$$

Using Eqs. (5) and (6) as constraints, Eq. (4) was integrated using the first-order Euler method to obtain steady-state solutions. We conducted simulations using various grid sizes and confirmed that our results were not affected by changing the grid size within the range of various grid sizes that we used.

Estimation of the *D/A* parameter value in the mouse brain. We compared the distribution of CSF tracer signals in the mouse brain and steady-state solutions of Eqs. (1) and (2) using various D/A values as written below. (Fig. 1).

As written in "Cisternal injection of a CSF tracer" in the Materials and Methods section, after the CSF tracer FITC-conjugated lysine-fixable 3 kDa dextran (Thermo Fisher Scientific, D3306) was injected into the cisterna magna of 1 month-old mice, tissue sections of the brain were prepared, and fluorescent images were taken using microscopes. To remove autofluorescence of the brain tissue, we calculated the average fluorescence intensity of the image without CSF tracer injection and subtracted it from the images with the CSF tracer. The resulting images showed the distribution of the CSF tracer in the brain.

Next, we performed simulations and then compared the steady-state solutions of the mathematical model and the distribution of the CSF tracer in the mouse brain section. We determined the similarity between these two using the mean square error of signal intensities, represented by E, as follows:

$$E = \int_{\psi_{\text{fit}}} \left(I_{\text{exp}}(\boldsymbol{x}) - \gamma c(\boldsymbol{x}) \right)^2 d\boldsymbol{x}. \tag{8}$$

In Eq. (7), $I_{\text{exp}}(\boldsymbol{x})$ was the fluorescence intensity at each position in experimental images (Fig. 1d). γ was a variable, and $\langle \ldots \rangle$ represents a statistical mean. We calculated a statistical mean in the region ψ_{fit}, which included gray matter, of the experimental image (Fig. 1d). The value of γ that minimized E was described as γ^*, and γ^* was obtained as follows:

$$\gamma^* = \frac{\int_{\psi_{\text{fit}}} I_{\text{exp}}(\boldsymbol{x}) c(\boldsymbol{x}) d\boldsymbol{x}}{\int_{\psi_{\text{fit}}} c(\boldsymbol{x})^2 d\boldsymbol{x}}. \tag{9}$$

E is a function using D/A and γ^* as variables. The value of D/A that minimizes E was described $(D/A)^*$. $(D/A)^*$ was obtained by calculating steady-state solutions at various D/A values and by comparing the solutions with the experimental image (Fig. 1c).

Finally, to confirm that our mathematical model properly reproduced the distribution of the CSF tracer in experimental brain sections, we compared signal intensities from the brain surface to deep cortical regions (Fig. 1e) between the experimental brain image and the steady-state solution of the mathematical model when $(D/A) = (D/A)^*$ and $\gamma = \gamma^*$ (Fig. 1d, e).

Numerical simulations of monkey and human brains. Using $(D/A)^*$ and γ^* determined using the mouse cerebral hemisphere, we predicted the distribution of CSF solutes in monkey and human cerebral hemispheres. The outlines of brain surfaces were manually extracted from images of coronal sections of monkey and human cerebral hemispheres (Supplementary Fig. 2), and images corresponding to the brain regions were created. Using these monkey and human brain images, simulations were performed to obtain steady-state distributions of CSF solutes. To investigate the importance of neuronal localization in the cerebral cortex, we created hypothetical brain images where neurons were homogeneously distributed in the entire cerebral hemispheres (Fig. 2a, e). In addition, to investigate the importance of cortical folds, we created hypothetical brain images without cortical folds (Fig. 3a and Supplementary Fig. 3a). Simulations were performed using these hypothetical brain images. The details are described in Supplementary Methods.

Estimations of parameters and the efficiency of glymphatic circulation in the ferret cerebral hemisphere. Based on our tracer experiments using ferrets, we expanded our mathematical model in Eqs. (1), (2), and (3) to the ferret cerebral hemisphere with different CSF influx efficiencies at gyri and sulci. The outline of the brain surface was manually extracted from images of coronal sections of the ferret cerebral hemisphere (Fig. 7a). To describe the different CSF influx efficiencies from gyral and sulcal surfaces, we manually divided the brain surface φ_0 into the gyral surface φ_g and the sulcal surface φ_s (Fig. 7a) and described the effective CSF solute concentrations in φ_g and φ_s to be c_g and c_s, respectively. Using these images, simulations were performed to estimate parameters and the efficiency of glymphatic circulation in the ferret cerebral hemisphere. Details are described in Supplementary Methods.

Reporting summary

Further information on research design is available in the Nature Portfolio Reporting Summary linked to this article.

Data availability

Source data are provided in this paper.

Code availability

All relevant codes are available from the corresponding authors upon request.

References

1. Kalebic, N. & Huttner, W. B. Basal progenitor morphology and neocortex evolution. *Trends. Neurosci.* **43**, 843–853 (2020).
2. Llinares-Benadero, C. & Borrell, V. Deconstructing cortical folding: genetic, cellular and mechanical determinants. *Nat. Rev. Neurosci.* **20**, 161–176 (2019).
3. Molnar, Z. et al. New insights into the development of the human cerebral cortex. *J. Anat.* **235**, 432–451 (2019).
4. Molnar, Z. et al. Comparative aspects of cerebral cortical development. *Eur. J. Neurosci.* **23**, 921–934 (2006).
5. Rakic, P. Evolution of the neocortex: a perspective from developmental biology. *Nat. Rev. Neurosci.* **10**, 724–735 (2009).
6. Sun, T. & Hevner, R. F. Growth and folding of the mammalian cerebral cortex: from molecules to malformations. *Nat. Rev. Neurosci.* **15**, 217–232 (2014).
7. Lui, J. H., Hansen, D. V. & Kriegstein, A. R. Development and evolution of the human neocortex. *Cell* **146**, 18–36 (2011).
8. Sherwood, C. C. et al. Evolution of increased glia-neuron ratios in the human frontal cortex. *Proc. Natl. Acad. Sci. USA* **103**, 13606–13611 (2006).
9. Herculano-Houzel, S. The glia/neuron ratio: how it varies uniformly across brain structures and species and what that means for brain physiology and evolution. *Glia* **62**, 1377–1391 (2014).
10. Shinmyo, Y., Hamabe-Horiike, T., Saito, K. & Kawasaki, H. Investigation of the mechanisms underlying the development and evolution of the cerebral cortex using gyrencephalic ferrets. *Front. Cell. Dev. Biol.* **10**, 847159 (2022).
11. Florio, M. & Huttner, W. B. Neural progenitors, neurogenesis and the evolution of the neocortex. *Development* **141**, 2182–2194 (2014).
12. Barkovich, A. J., Guerrini, R., Kuzniecky, R. I., Jackson, G. D. & Dobyns, W. B. A developmental and genetic classification for malformations of cortical development: update 2012. *Brain* **135**, 1348–1369 (2012).
13. Guerrini, R. & Marini, C. Genetic malformations of cortical development. *Exp. Brain Res.* **173**, 322–333 (2006).
14. Ross, M. E. & Walsh, C. A. Human brain malformations and their lessons for neuronal migration. *Annu. Rev. Neurosci.* **24**, 1041–1070 (2001).
15. Francis, F. et al. Human disorders of cortical development: from past to present. *Eur. J. Neurosci.* **23**, 877–893 (2006).

16. Poduri, A., Evrony, G. D., Cai, X. & Walsh, C. A. Somatic mutation, genomic variation, and neurological disease. *Science* **341**, 1237758 (2013).
17. de Juan Romero, C., Bruder, C., Tomasello, U., Sanz-Anquela, J. M. & Borrell, V. Discrete domains of gene expression in germinal layers distinguish the development of gyrencephaly. *EMBO J.* **34**, 1859–1874 (2015).
18. Matsumoto, N., Tanaka, S., Horiike, T., Shinmyo, Y. & Kawasaki, H. A discrete subtype of neural progenitor crucial for cortical folding in the gyrencephalic mammalian brain. *ELife* **9**, e54873 (2020).
19. Shinmyo, Y. et al. Folding of the cerebral cortex requires Cdk5 in upper-Layer neurons in gyrencephalic mammals. *Cell Rep.* **20**, 2131–2143 (2017).
20. Shinmyo, Y. et al. Localized astrogenesis regulates gyrification of the cerebral cortex. *Sci. Adv.* **8**, eabi5209 (2022).
21. Mestre, H., Mori, Y. & Nedergaard, M. The brain's glymphatic system: current controversies. *Trends Neurosci.* **43**, 458–466 (2020).
22. Iliff, J. J. et al. A paravascular pathway facilitates CSF flow through the brain parenchyma and the clearance of interstitial solutes, including amyloid beta. *Sci. Transl. Med.* **4**, 147ra111 (2012).
23. Mestre, H. et al. Aquaporin-4-dependent glymphatic solute transport in the rodent brain. *ELife* **7**, e40070 (2018).
24. Munk, A. S. et al. PDGF-B is required for development of the glymphatic system. *Cell Rep.* **26**, 2955–2969 (2019).
25. Harrison, I. F. et al. Impaired glymphatic function and clearance of tau in an Alzheimer's disease model. *Brain* **143**, 2576–2593 (2020).
26. Peng, W. et al. Suppression of glymphatic fluid transport in a mouse model of Alzheimer's disease. *Neurobiol. Dis.* **93**, 215–225 (2016).
27. Toh, C. H. & Siow, T. Y. Glymphatic dysfunction in patients with ischemic stroke. *Front. Aging Neurosci.* **13**, 756249 (2021).
28. Gaberel, T. et al. Impaired glymphatic perfusion after strokes revealed by contrast-enhanced MRI: a new target for fibrinolysis? *Stroke* **45**, 3092–3096 (2014).
29. Ferrara, M. et al. Glymphatic system a window on TBI pathophysiology: a systematic review. *Int. J. Mol. Sci.* **23**, 9138 (2022).
30. Iliff, J. J. et al. Impairment of glymphatic pathway function promotes tau pathology after traumatic brain injury. *J. Neurosci.* **34**, 16180–16193 (2014).
31. Fernandez, V., Llinares-Benadero, C. & Borrell, V. Cerebral cortex expansion and folding: what have we learned? *EMBO J.* **35**, 1021–1044 (2016).
32. Hofman, M. A. Evolution of the human brain: when bigger is better. *Front. Neuroanat.* **8**, 15 (2014).
33. Matsumoto, N., Shinmyo, Y., Ichikawa, Y. & Kawasaki, H. Gyrification of the cerebral cortex requires FGF signaling in the mammalian brain. *ELife* **6**, e29285 (2017).
34. Xia, M., Yang, L., Sun, G., Qi, S. & Li, B. Mechanism of depression as a risk factor in the development of Alzheimer's disease: the function of AQP4 and the glymphatic system. *Psychopharmacology* **234**, 365–379 (2017).
35. Alshuhri, M. S., Gallagher, L., Work, L. M. & Holmes, W. M. Direct imaging of glymphatic transport using $H_2^{17}O$ MRI. *JCI Insight* **6**, e141159 (2021).
36. Mota, B. et al. White matter volume and white/gray matter ratio in mammalian species as a consequence of the universal scaling of cortical folding. *Proc. Natl. Acad. Sci. USA* **116**, 15253–15261 (2019).
37. Van Essen, D. C. et al. Cerebral cortical folding, parcellation, and connectivity in humans, nonhuman primates, and mice. *Proc. Natl. Acad. Sci. USA* **116**, 26173–26180 (2019).
38. Bechet, N. B., Shanbhag, N. C. & Lundgaard, I. Glymphatic pathways in the gyrencephalic brain. *J. Cereb. Blood Flow Metab.* **41**, 2264–2279 (2021).
39. Gonzalez-Lagos, C., Sol, D. & Reader, S. M. Large-brained mammals live longer. *J. Evol. Biol.* **23**, 1064–1074 (2010).
40. Kawasaki, H., Iwai, L. & Tanno, K. Rapid and efficient genetic manipulation of gyrencephalic carnivores using in utero electroporation. *Mol. Brain* **5**, 24 (2012).
41. Hablitz, L. M. et al. Increased glymphatic influx is correlated with high EEG delta power and low heart rate in mice under anesthesia. *Sci. Adv.* **5**, eaav5447 (2019).
42. Xavier, A. L. R. et al. Cannula implantation into the cisterna magna of rodents. *J. Vis. Exp.* **135**, e57378 (2018).
43. Guo, S. et al. Akt/aquaporin-4 signaling aggravates neuropathic pain by activating astrocytes after spinal nerve ligation in rats. *Neuroscience* **482**, 116–131 (2022).
44. Iwai, L. et al. FoxP2 is a parvocellular-specific transcription factor in the visual thalamus of monkeys and ferrets. *Cereb. Cortex* **23**, 2204–2212 (2013).
45. Hayakawa, I. & Kawasaki, H. Rearrangement of retinogeniculate projection patterns after eye-specific segregation in mice. *PLoS ONE* **5**, e11001 (2010).
46. Toda, T. et al. Birth regulates the initiation of sensory map formation through serotonin signaling. *Dev. Cell.* **27**, 32–46 (2013).
47. Dinh Duong, T. A. et al. FGF signaling directs the cell fate switch from neurons to astrocytes in the developing mouse cerebral cortex. *J. Neurosci.* **39**, 6081–6094 (2019).
48. Kawasaki, H. et al. Induction of midbrain dopaminergic neurons from ES cells by stromal cell-derived inducing activity. *Neuron* **28**, 31–40 (2000).
49. Ebisu, H., Iwai-Takekoshi, L., Fujita-Jimbo, E., Momoi, T. & Kawasaki, H. Foxp2 regulates identities and projection patterns of thalamic nuclei during development. *Cereb. Cortex* **27**, 3648–3659 (2017).
50. Kawasaki, H., Crowley, J. C., Livesey, F. J. & Katz, L. C. Molecular organization of the ferret visual thalamus. *J. Neurosci.* **24**, 9962–9970 (2004).
51. Morita, K. et al. BMP signaling alters aquaporin-4 expression in the mouse cerebral cortex. *Sci. Rep.* **11**, 10540 (2021).
52. Yan, T. et al. HUCBCs increase angiopoietin 1 and induce neurorestorative effects after stroke in T1DM rats. *CNS Neurosci. Ther.* **20**, 935–944 (2014).
53. Johnson, L. et al. A novel method to quantify perivascular space enlargement near the syrinx in a rodent model of post-traumatic syringomyelia. *Sci. Rep.* **13**, 15043 (2023).

Acknowledgements

We are grateful to Zachary Blalock and the Kawasaki lab members for their helpful support, critical discussions, and comments on this manuscript. This work was supported by Grant-in-Aid for Scientific Research from the Ministry of Education, Culture, Sports, Science and Technology (MEXT); Japan Agency for Medical Research and Development (AMED) [Grant No. JP24wm0625112 to H.K.]; the Japan Science and Technology Agency (JST), CREST [Grant No. JPMJCR1921 to S.O.]; the Japan Society for the Promotion of Science (JSPS), KAKENHI [Grants No. 23H00389 to HK, 21K19306 to H.K., 20H03338 to H.K., 23H02586 to Y.S., 23K27277 to Y.S., 20H03351 to Y.S., 21K19307 to Y.S., 22K18397 to M.N., 22H05170 to S.O.]; the World Premier International Research Center Initiative, MEXT to S.O.; Takeda Science Foundation to H.K. and Y.S.; the Uehara Memorial Foundation to H.K.; the Naito Foundation to H.K.; Kanazawa University SAKIGAKE Project 2018 to H.K. and Kanazawa University CHOZEN Project to H.K. These results were obtained from research (No. 23001 to H.K.) commissioned by the National Institute of Information and Communications Technology (NICT), Japan. N.K. and I.S. are supported by the WISE Program for Nano-Precision Medicine, Science, and Technology at Kanazawa University from MEXT and by Research Fellowships for Young Scientists of the Japan Society for the Promotion of Science.

Author contributions

N.K., S.O., and H.K. designed the experiments. N.K., I.S., K.S., T.H.H., Y.S., and M.N. collected the data. N.K., I.S., S.O., and H.K. wrote the manuscript.

Competing interests

The authors declare that no competing interests exist.

Additional information

Supplementary information The online version contains supplementary material available at https://doi.org/10.1038/s41467-024-54372-1.

Correspondence and requests for materials should be addressed to Satoru Okuda or Hiroshi Kawasaki.

Peer review information *Nature Communications* thanks Nereo Kalebic, Douglas Kelley and the other anonymous reviewer(s) for their contribution to the peer review of this work. A peer review file is available.

Reprints and permissions information is available at http://www.nature.com/reprints

Publisher's note Springer Nature remains neutral with regard to jurisdictional claims in published maps and institutional affiliations.

Open Access This article is licensed under a Creative Commons Attribution-NonCommercial-NoDerivatives 4.0 International License, which permits any non-commercial use, sharing, distribution and reproduction in any medium or format, as long as you give appropriate credit to the original author(s) and the source, provide a link to the Creative Commons licence, and indicate if you modified the licensed material. You do not have permission under this licence to share adapted material derived from this article or parts of it. The images or other third party material in this article are included in the article's Creative Commons licence, unless indicated otherwise in a credit line to the material. If material is not included in the article's Creative Commons licence and your intended use is not permitted by statutory regulation or exceeds the permitted use, you will need to obtain permission directly from the copyright holder. To view a copy of this licence, visit http://creativecommons.org/licenses/by-nc-nd/4.0/.

© The Author(s) 2024